Int. J. Multiphase Flow Vol. 18, No. 4, pp. 495–516, 1992
Printed in Great Britain.

0301-9322/92 $5.00 + 0.00

EXPERIMENTAL CHARACTERIZATION OF VISCOUS FILM FLOWS OVER COMPLEX SURFACES

L. ZHAO and R. L. CERRO†
Chemical Engineering Department, University of Tulsa, Tulsa, OK 74104, U.S.A.

(Received 12 June 1991; in revised form 23 March 1992)

Abstract—Ordered packings are made of a variety of materials such as ceramics, metal and plastics, and shaped to a wide spectrum of macro- and micro-structures. Macro-structures, usually in the form of corrugations, sustain good liquid–vapor contact with low overall pressure drop. Micro-structures in the way of surface treatment, metal gauze and surface indentations, help to increase the stability of the liquid film by preventing breakups and dry patches. An experimental research program was carried out in order to characterize the mechanics of viscous flows over model complex surfaces. Film thickness profiles, streamline patterns and free-surface velocities were measured for a variety of surface shapes and fluids. These results are important in the understanding of the interaction of capillary, viscous and gravity forces on the shaping of the film free surface. The position of the liquid film interface was found, in general, to have the same period as the wavy solid but amplitude and phase-shift vary with flow parameters. Free-surface profiles are patterned around the shape of the solid surfaces but their amplitude decreased with increasing Nusselt film thickness. Free-surface velocity measurements show peaks of velocity larger than the maximum predicted for vertical films. These peaks are associated to a minimum in film thickness and are detected in regions where there is an inflexion point in free surface curvature. Three parameters, Nusselt film thickness, Reynolds number and Capillary number, are necessary to characterize accurately these liquid film flows.

Key Words: viscous film flow, packings, free surfaces

1. COLUMN PACKINGS MADE OF COMPLEX SURFACES

The use of packing materials to improve vapor–liquid contact in mass transfer columns has widespread applications in chemical engineering. For a scholarly historical introduction and description of packing functionality, the reader is referred to a recent review by de Santos *et al.* (1991). Ordered packings, such as those constructed of corrugated sheet metal, are typical of a variety of commercial heat and mass transfer devices. The use of ordered packings as packing materials has greatly increased in the last two decades (Bravo *et al.* 1984; Kurtz *et al.* 1991). Ordered packings have a well-defined structure and usually outperform random packings and tray towers in difficult separations with pressure gradient constraints, low relative volatilities and/or small liquid holdup. Better mass transfer efficiency at low pressure gradients between the bottom and top of gas–liquid contacting columns usually results in a smaller energy consumption for a comparable duty than random packings or plate columns.

Ordered packings are usually made of corrugated sheets that may have been chemically treated or mechanically roughened in order to improve wetting and promote film stability. Hence, two types of structures can be identified associated to ordered packings: first, there is a *macro-structure* generated by corrugation (a schematic representation of a triangular cross section and its vertical arrangement is shown in figure 1; the characteristic size of corrugations, b, is of the order of 0.01–0.03 m); the second type of structure is the *micro-structure*, which is associated with the metal surface treatment and its characteristic size is of the order of 0.001 m. The micro-structure adopts the form of gauze, surface indentations, chemical treatment (to generate a specific crystal structure) etc.

An experimental program was carried out in order to characterize flow performance of viscous films over several complex surfaces. Although there are a number of papers on experimental characterization of falling films (Fulford 1964), the authors know of no published data on flow over solid surfaces with a periodic shape. The surfaces used in these experiments were designed to

†To whom all correspondence should be addressed.

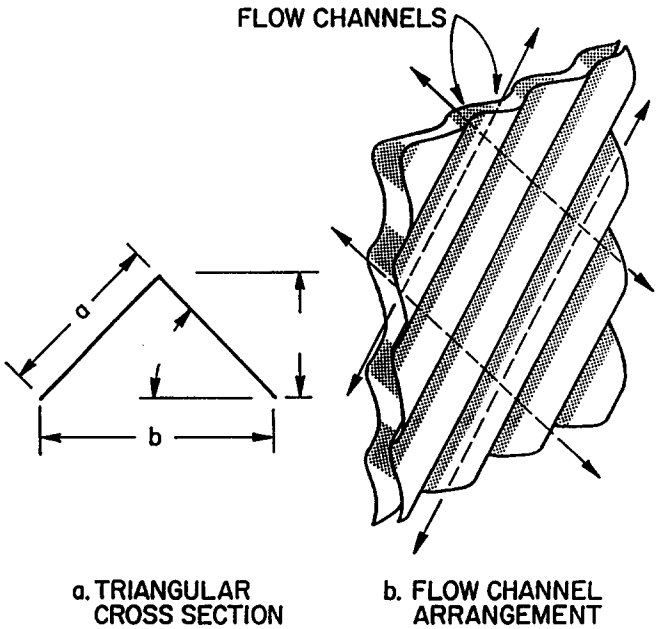

Figure 1. Schematic representation of the corrugated sheets used in the fabrication of ordered packings.

simulate the main features of surfaces used in industrial practice. A combination of different surface shapes and fluids enabled a study covering a wide range of film amplitude ratios, Capillary and Reynolds numbers. Relevant parameters for the surfaces studied are indicated in figure 2. Figure 2(a) shows a surface consisting of a stack of cylindrical rods. The rods are 3.175×10^{-3} m in diameter (d) and are stacked vertically with a line of contact along the tangent parallel to the cylinder axis. The wavelength of this surface is equal to the rod diameter. The amplitude is taken

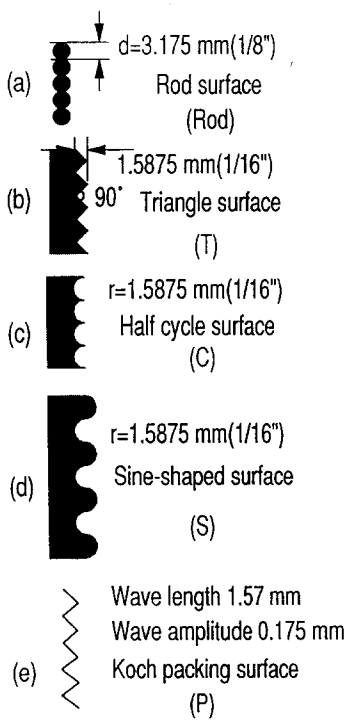

Figure 2. Definition of relevant parameters for the complex surfaces used in the experiments. **Rod**, **T** and **C** surfaces were made of brass. **S** surfaces were made of brass and acrylic. The industrial **P** surface was made of stainless steel.

to be one-half the distance from top to bottom of the periodic surface shapes. In the case of the **rod** surface, the amplitude is equal to one-half the radius of the rods, $r = 1.5875 \times 10^{-3}$ m and the ratio of amplitude/wavelength is $\lambda = r/(2d) = 0.25$. The rods were made out of the same type of phosphorous brass used in making the machined surfaces. The main characteristic of the **rod** surface is the presence of cusp-like wedges generated by the points of contact along the contacting lines of the cylindrical rods. These wedges have a strong effect on the shape of the streamlines and accumulate fluid even when there is no flow.

The second type of surface has a triangular cross section and is shown in figure 2(b). The face of the surface has been machined on a 3/16″ plate brass to generate triangle-shaped grooves. The upper and lower angles are both 90° and the wave amplitude is one-half the height of the triangles, $b = 0.79375 \times 10^{-3}$ m. The wavelength, that is the distance between two consecutive vertices is $a = 3.175 \times 10^{-3}$ m. The ratio of amplitude/wavelength is $\lambda = 0.25$. This surface has a shape very similar to an industrial packing material provided by Koch Engineering Co. (Wichita, KS) and shown in figure 2(e). The Koch surface, hereafter called the **P** surface, was made of stainless steel and has a wavelength $a = 1.57 \times 10^{-3}$ m and a wave amplitude $b = 0.175 \times 10^{-3}$ m. The corresponding vertex angle is 132° and $\lambda = 0.11$. It should be noted that this is a micro-structure for the Koch surface since it is usually corrugated to sine-shape or triangular shapes with a wavelength of about 0.02 m.

The third type of surface, denoted as the **C**-shaped surface, is shown in figure 2(c). This surface is made of brass plate by machining grooves on the surface with a round tool. The radius of the machine tool is $r = 1.5875 \times 10^{-3}$ m and the space between two grooves is 0.2×10^{-3} m. The resulting wavelength is slightly larger than the diameter of the grooves, $a = 3.275 \times 10^{-3}$ m and $\lambda = 0.2425$.

The fourth surface is an approximation to a sine wave and is shown in figure 2(d). The surface is made of a sequence of semi-circular grooves and convex semi-circular ridges. The radius of the grooves and ridges is $r = 1.5875 \times 10^{-3}$ m. The amplitude of the waves is twice the radius, $b = 1.5875 \times 10^{-3}$ m, and the wavelength $a = 6.35 \times 10^{-3}$ m. Hence, the ratio of amplitude/wavelength $\lambda = 0.25$. The shape of the surface slightly departs from a sine wave. Nevertheless, it will be referred to as the sine-shaped or **S** surface. The **S** surface used in these experiments was made out of brass.

An important parameter related to the geometry of these complex surfaces is defined as the ratio of the Nusselt liquid film thickness to the solid surface amplitude:

$$\delta = \frac{h^*}{A}. \qquad [1]$$

Three different fluids were used in these experiments: glycerin, glycerin–water solutions and silicone oil. Two types of glycerin are listed, a commercial brand listed as glycerin A and a purer form listed as glycerin B. The only difference between these two types of glycerin is their water content which in turn affects viscosity. This is a problem of using pure glycerin, since it is hygroscopic and viscosity will change with time if reused. For the short time that the glycerin is exposed to air on the model surface, properties can be assumed constant. The glycerin–water solutions had ratios of 2:1 and 1:1. The most relevant properties of these fluids are shown in table 1. For all experimental surfaces, the ratio of Nusselt liquid film thickness/solid surface amplitude parameter, δ, falls between 0.1 and 1 except for the experiments on the **P** surface, where $2.29 < \delta < 5.09$.

2. EXPERIMENTAL SETUP

Film thickness measurements, free-surface measurements and flow visualization techniques were used to unveil details of the flow patterns and relevant flow parameters. Flow visualization

Table 1. Relevant properties of the fluids used in the experiments

Fluid	Glycerin A	Glycerin B	Glycerin–water 2:1	Glycerin–water 1:1	Silicone oil
Density (kg/m^3)	1261	1265	1227	1139	969
Viscosity (Pa·s)	0.45	0.938	0.0195	0.0068	0.0885
Dynamic viscosity (m^2/s)	3.6×10^{-4}	7.42×10^{-4}	1.59×10^{-5}	5.97×10^{-6}	9.12×10^{-5}
Surface tension (N/m)	0.0625	0.06	0.0671	0.0696	0.0214

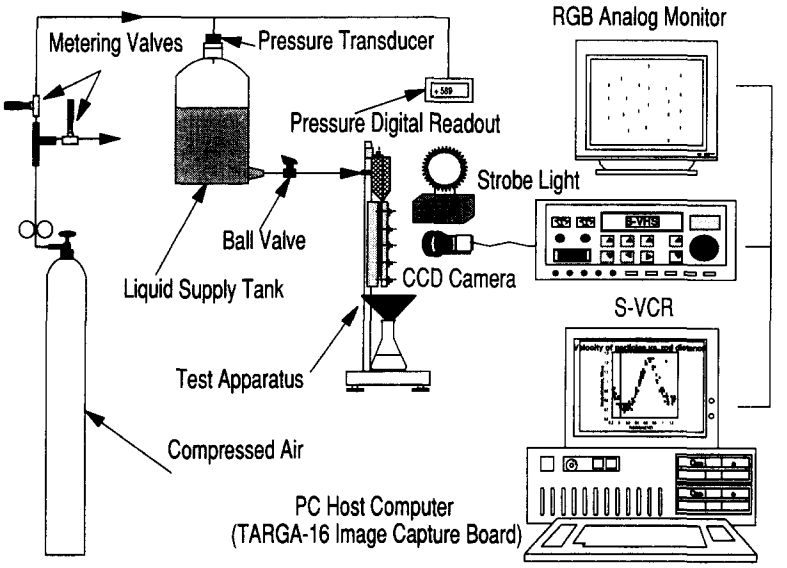

Figure 3. Schematic view of the experimental setup. Details of the equipment and the image analysis system can be found in Camp *et al.* (1990).

techniques were described by Merzkirch (1987) and more recently by Yang (1989). Merzkirch (1987) describes various flow visualization techniques such as seeding with smoke, tracer particles etc. Yang (1989) summarizes all major techniques of flow visualization and demonstrates their application in fields of science and technology.

The experimental setup, shown schematically in figure 3, consists of three major components: (1) flow distributor, test surface and flow metering devices; (2) measuring and flow visualization components; and (3) a computer-based image capture and image analysis system. The flow distributor and test surface, as well as all measuring and flow visualization components, were rigidly mounted on a vibration-free optical table from Oriel Corp. (Stratford, CT). An enlarged view of the flow distributor is shown in figure 4. Test surfaces 0.1 m wide and 0.15 m high were set in a vertical position directly under the flow distributor. For all test surfaces there were at least 20 full wave periods from top to bottom of the solid surface. Measurements were made in the lower part of the test surface, i.e. at least 10–15 wave periods downstream of the feeding line, to assure that a fully developed flow was present. The surfaces were clamped on the side. During the flow

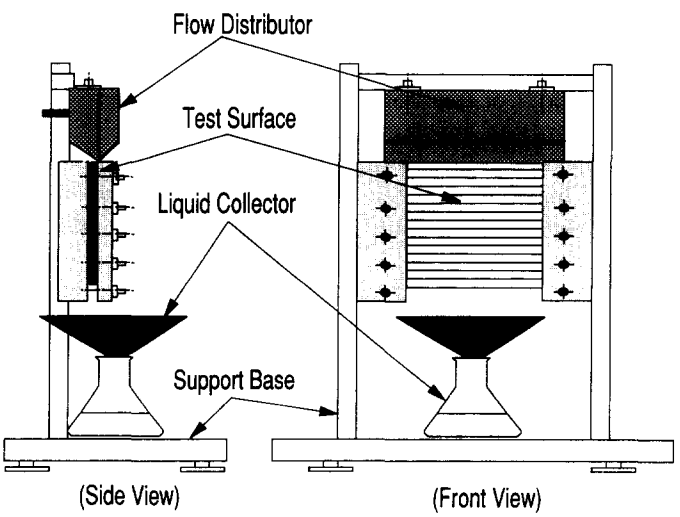

Figure 4. Schematic view of the flow distributor and experimental model surface. The flow distributor in the top creates a very narrow curtain of liquid that is immediately picked up by the top of the model surface.

visualization experiments, one of the clamps was removed in order to have a closer side-view. The very narrow slit of the flow distributor, 0.001 m wide, was designed to give a uniform flow rate across the surface for all ranges of flow rates. The flow rate was measured by collecting the liquid dripping at the bottom of the test surface and measuring volumes in a graduated flask. For small flow rates, the collected liquid was weighed and volumetric flow rates computed using the liquid density.

The first set of experiments was designed to measure the liquid film thickness distribution on the surface as a function of position along the solid surface. A detailed sketch of the film thickness measuring setup is shown in figure 5. A very thin (0.2×10^{-3} m) sewing needle was welded on the end of a syringe needle. The sewing needle was filed down to end on a 0.01×10^{-3} m tip. The ensemble was secured on an x–y precision translator with a minimum register of $\pm 10^{-6}$ m. It is estimated that these measurements are precise up to 0.01×10^{-3} m. The x–y precision translator was mounted on an Oriel tubular bench with a horizontal translator. The tubular bench was then secured on the optical table. The measuring ensemble could be positioned at any point of the solid surface. Precise vertical and horizontal needle displacements were measured using the precision micrometers. The back of the brass plate and the needle were connected to a laboratory ohmmeter. Due to the large difference in electrical conductivity between air and the glycerin–water solutions, it was possible to detect the position where the needle touched the liquid surface and then the position where the needle touched the metal surface. Since the electrical conductivity of the oil is very low, when silicone oil was used the position of the air–liquid interface was detected with a combination of side-lighting and a video camera zoomed-in on the liquid surface.

It is possible to align the brass plate and the tubular bench in such a way that their axes are almost parallel but is impossible to make them perfectly parallel. This problem is avoided by measuring the position of the free surface and the position of the metal surface at every point of measurement. The problem of a non-perpendicular approach to the surface remains, but by measuring the position of two consecutive maxima of the solid surface the error was estimated to be $<0.4°$ between the two axes.

The second set of experiments consisted of mapping streamline patterns in a vertical cross section of the liquid film. Streamlines were generated by the streak image of particles as they moved through the field of vision of a video camera when illuminated by a sheet of laser light. The particles used were aluminum spheres 20 μm in diameter. In order to get a very low particle concentration, aluminum particles were seeded in the fluid 1 week prior to use and allowed to sediment. The bottom part of the resulting fluid was discarded. Theory and experiments have proven that for low seeding densities the fluid velocity field is not affected by the particles (Merzkirch 1987). A laser sheet, 10^{-4} m thick, was created with a combination of collimating and cylindrical lenses and could

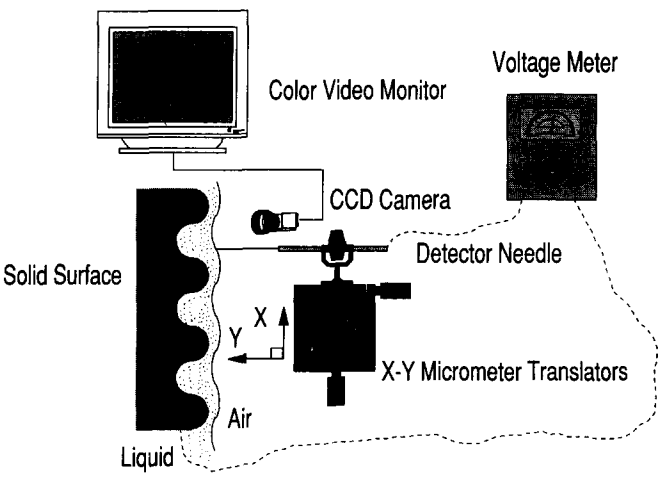

Figure 5. Schematic view of the film thickness measurement setup. The ohmmeter was used to detect contact with the metal solid surface and the free surface of the conducting fluids. When silicone oil was used, the image system showed an amplified close-up of the liquid surface that allowed detection of the point of contact.

be positioned at any point of the test surface. Seeding density was very low such that no more than 4 or 5 particles were visible in any given video frame. The CCD video camera has a shutter speed of 1/30 s. The composite images of the streamline patterns were then generated by running the video images at normal speed on a flat 24″ video monitor and taking a picture of the monitor with a still camera open for intervals of several seconds.

Free-surface velocities were measured using particle image velocimetry (PIV) (Adrian 1984). Particles traveling on the free surface of a fluid illuminated with a stroboscopic light generate particle tracks in multiple exposure photographs. In particle image photographs, the streak length or the track length can be used to determine velocity vectors in the flow field. Particles were sprinkled on top of the free surface of the liquid coming out of the flow distributor. Sprinkling is done lightly so that the particles do not penetrate into the film. Two types of particles were used, aluminum spheres 20 μm in diameter and spherules of ion exchange resin DOWEX-1 from Sigma Chemical Co. (St Louis, MO). The spherules were 200–400 dry mesh and of very low density. A stroboscopic, high-frequency lamp was used as a light source and a high-resolution CCD camera with an exposure of 1/60 s was used to capture the images. As a result, every particle leaves several streaks in one video frame. Video frames were then digitized using a TARGA-16 frame grabber in an Intel 80286 16 MHz computer. The resulting digital frames were analyzed using a program that computes the velocity of the particles using the distance traveled between streaks. Details of the image analysis system can be found in Camp *et al.* (1990).

3. FILM THICKNESS MEASUREMENTS

Measurement of the film thickness was done only after the flows reached steady state. A visual indication of steady state was the absence of waves or bubbles, as observed in the monitor screen, and a constant flow rate—indicated by collecting liquid samples at regular intervals. The micrometer readout was set to zero and the micrometer with the needle was then moved very slowly towards the liquid surface. When water and glycerin were used, the point of contact of the needle was detected by a jump in the electrical conductivity of the circuit shown in figure 5. When silicone oils were used, the point of contact was detected by observing the free surface laterally with a highly amplified video camera. After the first point of contact, the needle was moved forward again until it touched the metal surface. At this point, another jump in conductivity indicated contact between the needle and the metal surface. The needle was then retracted and a precision micrometer used to move it vertically along the surface. All measurements were done from bottom to top. By detecting contacts with both the free and solid surfaces it was assured that no errors due to non-parallel alignment of the solid surface and the micrometer setup affected the measurement of film thickness. For non-wetting systems, such as glycerin and water on a brass surface, a polymer edge was used to pin the contact lines on the surface of the brass plate. In this way, the width of the solid surface covered by the film was kept constant for the whole length of the test surface.

The experimental conditions are summarized in tables 2–6. u_m^* and h^* are the theoretical Nusselt free-surface velocity and film thickness, respectively, for a film flowing on a flat vertical surface. These parameters are defined as follows:

$$u_m^* = \frac{\rho g (h^*)^2}{2\mu} \qquad [2]$$

$$h^* = \sqrt[3]{\frac{3\mu q}{\rho g}}, \qquad [3]$$

where μ is the fluid viscosity (Pa·s), q is the liquid flow rate per unit width, ρ is the fluid density (kg/m^3) and g is the acceleration of gravity (m/s^2). The Reynolds and Capillary numbers are computed using the following equations:

$$\mathrm{Re} = \frac{\rho q}{\mu} \qquad [4]$$

and

$$\mathrm{Ca}_m = \frac{\mu u_m^*}{\sigma}. \qquad [5]$$

Table 2. Parameters for the experimental runs over a **P** surface

No.	Liquid	q ($m^3/s \cdot m$)	h^* (mm)	u_m^* (mm/s)	Re	Ca_m
1P	W–G = 1:2	1.452E − 04	0.89	244.51	9.1246	0.0711
2P	W–G = 1:2	6.056E − 05	0.67	136.52	3.8070	0.0397
3P	Silicone oil	4.517E − 06	0.50	13.52	0.0495	0.0557
4P	Silicone oil	3.946E − 06	0.48	12.35	0.0433	0.0509
5P	Silicone oil	2.279E − 06	0.40	8.57	0.0250	0.0353
6P	Glycerol B	2.122E − 06	0.78	4.06	0.0029	0.0609
7P	Glycerol B	1.684E − 06	0.73	3.48	0.0023	0.0522
8P	Glycerol B	6.906E − 07	0.54	1.92	0.0009	0.0288

Table 3. Parameters for the experimental runs over an **S** surface

No.	Liquid	q ($m^3/s \cdot m$)	h^* (mm)	u_m^* (mm/s)	Re	Ca_m
1S	Silicone oil	3.529E − 05	0.99	53.22	0.3870	0.2195
2S	Silicone oil	1.511E − 05	0.75	30.23	0.1657	0.1247
3S	Silicone oil	1.171E − 05	0.69	25.51	0.1284	0.1052
4S	Silicone oil	8.114E − 06	0.61	19.97	0.0890	0.0824
5S	Silicone oil	2.413E − 06	0.41	8.90	0.0265	0.0367
6S	Silicone oil	2.017E − 06	0.38	7.90	0.0221	0.0326
7S	Silicone oil	1.817E − 06	0.37	7.36	0.0199	0.0304
8S	Silicone oil	1.764E − 06	0.37	7.22	0.0193	0.0298
9S	Silicone oil	5.441E − 07	0.25	3.30	0.0060	0.0136
10S	Silicone oil	3.910E − 07	0.22	2.64	0.0043	0.0109
11S	Glycerol A	5.416E − 06	0.86	9.41	0.0139	0.0738
12S	Glycerol A	3.617E − 06	0.75	7.19	0.0093	0.0564
13S	Glycerol A	2.670E − 06	0.68	5.87	0.0069	0.0460
14S	Glycerol A	1.843E − 06	0.60	4.59	0.0047	0.0360
15S	Glycerol A	1.463E − 06	0.56	3.93	0.0038	0.0308
16S	Glycerol B	1.382E − 06	0.68	3.05	0.0019	0.0458
17S	Glycerol B	1.103E − 06	0.63	2.62	0.0015	0.0394
18S	Glycerol B	8.388E − 07	0.58	2.19	0.0011	0.0328
19S	Glycerol B	7.748E − 07	0.56	2.07	0.0010	0.0311

Table 4. Parameters for the experimental runs over a **C** surface

No.	Liquid	q ($m^3/s \cdot m$)	h^* (mm)	u_m^* (mm/s)	Re	Ca_m
1C	W–G = 1:2	7.643E − 05	0.72	159.43	4.8045	0.0464
2C	W–G = 1:2	5.569E − 05	0.65	129.10	3.5009	0.0375
3C	Silicone oil	1.173E − 05	0.69	25.54	0.1287	0.1053
4C	Silicone oil	3.138E − 06	0.44	10.60	0.0344	0.0437
5C	Silicone oil	2.048E − 06	0.39	7.98	0.0225	0.0329
6C	Silicone oil	1.979E − 06	0.38	7.80	0.0217	0.0321
7C	Glycerol B	1.776E − 06	0.74	3.60	0.0024	0.0541
8C	Glycerol B	1.592E − 06	0.71	3.35	0.0021	0.0503
9C	Glycerol B	9.169E − 07	0.59	2.32	0.0012	0.0348
10C	Glycerol B	4.458E − 07	0.47	1.43	0.0006	0.0215

Table 5. Parameters for the experimental runs over a **T** surface

No.	Liquid	q ($m^3/s \cdot m$)	h^* (mm)	u_m^* (mm/s)	Re	Ca_m
1T	Silicone oil	3.684E − 05	1.01	54.76	0.4039	0.2258
2T	Silicone oil	3.355E − 05	0.98	51.45	0.3678	0.2122
3T	Silicone oil	2.832E − 06	0.43	9.90	0.0310	0.0408
4T	Silicone oil	2.557E − 06	0.41	9.25	0.0280	0.0381
5T	Silicone oil	2.285E − 06	0.40	8.58	0.0251	0.0354
6T	Silicone oil	2.170E − 06	0.39	8.29	0.0238	0.0342
7T	Silicone oil	9.586E − 07	0.30	4.81	0.0105	0.0198
8T	Silicone oil	2.753E − 07	0.20	2.09	0.0030	0.0086

Table 6. Parameters for the experimental runs over a **rod** surface

No.	Liquid	q ($m^3/s \cdot m$)	h^* (mm)	u_m^* (mm/s)	Re	Ca_m
1R	W–G = 1:2	3.879E − 05	0.57	101.44	2.4383	0.0295
2R	W–G = 1:2	3.585E − 05	0.56	96.25	2.2536	0.0280
3R	W–G = 1:2	3.582E − 05	0.56	96.20	2.2519	0.0280
4R	Silicone oil	2.833E − 05	0.92	45.97	0.3107	0.1896
5R	Silicone oil	1.648E − 06	0.36	6.90	0.0181	0.0285
6R	Silicone oil	3.412E − 07	0.21	2.42	0.0037	0.0100

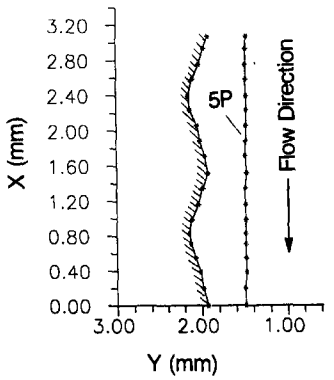

Figure 6. Film thickness data for the flow of silicone oil on a **P** surface; $\delta = 2.29$. The free surface is nearly flat.

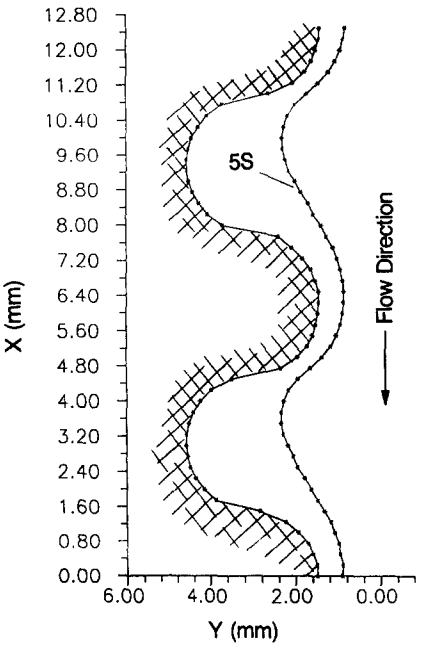

Figure 7. Film thickness data for an **S** surface; $\delta = 0.258$. The free surface is periodic and has the same wavelength as the solid surface.

When the Nusselt film thickness, h^*, is of the same order or larger than the amplitude of the solid surface structure, i.e. for values of $\delta > 1$, the free-surface profile becomes nearly flat. See figure 6 for a flow of silicone oil over a **P** surface. In these experiments $2.29 < \delta < 5.09$. At smaller flow rates, i.e. for $0.1 < \delta < 1$, the free surface becomes periodic with a wavelength of the same length as the wavelength of the solid surface. See figure 7 for the flow of silicone oil over an **S** surface. There is no sharp transition from flat profiles to periodic profiles. The nearly flat surfaces found for larger values of δ are wavy surfaces with a very small wave amplitude. Periodic surfaces slowly evolve as the flow rate increases. There are no experimental results for very small ratios of film thickness/amplitude of the solid surface structure, i.e. for $\delta < 0.1$. However, at very low values of δ liquid surface profiles have a period equal to one-half the period of the solid surface and the film closely follows the changes in inclination of the solid surface with respect to gravity (Zhao & Cerro 1988).

The correlation of the film thickness data is based on three parameters: (1) Nusselt film thickness, h^*, defined by [2]; (2) Reynolds number, Re, defined by [4]; and (3) Capillary number, Ca, defined by [5]. These parameters represent the three conditions that, during the experiments, can be chosen arbitrarily for a given type of solid surface and inclination: (1) flow rate, q; (2) kinematic viscosity, ν; and (3) surface tension, σ. Figures 8–10 show the effect of varying these three parameters. Unfortunately, to vary one parameter at a time while keeping the other two parameters constant during the experiments would be extremely difficult. Thus, it can only be shown that none of the three parameters can be used independently to correlate the experimental results. Figure 8 compares the free-surface profile of a 0.0885 Pa·s silicone oil and glycerin B ($\mu = 0.938$ Pa·s) over an **S** surface. The film thickness to amplitude ratio is the same in both cases, $\delta = 0.43$. There are appreciable differences in the film thickness profile and the minimum radius of curvature of the free surfaces. For silicone oil, Re and Ca are larger than the respective values for glycerin. As a consequence, the minimum radius of curvature of the free surface in the silicone oil profile is smaller than the corresponding minimum on the glycerin surface. Figure 9 compares the free-surface profiles for the flow of silicone oil and glycerin A over an **S** surface. In this case, Re is nearly constant but h^* and Ca differ considerably from one experiment to the other. The difference in free-surface profiles is quite dramatic, indicating that Re could not be used as the sole parameter to correlate these experimental results. Finally, figure 10 is used to compare free-surface profiles

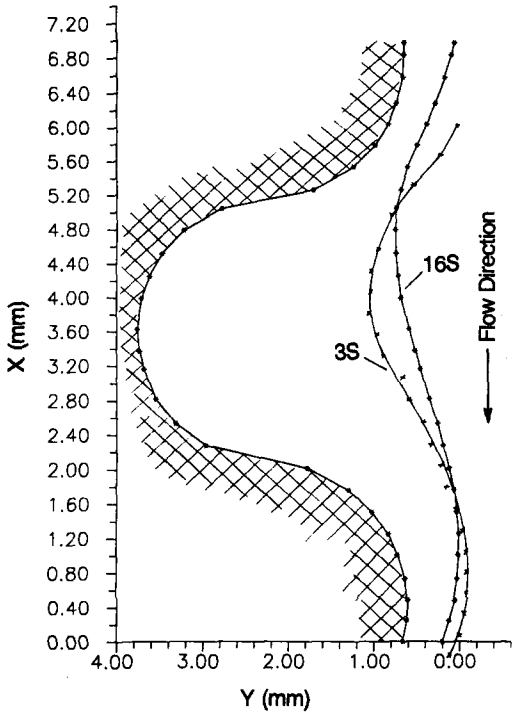

Figure 8. Film thickness data for two experimental runs with similar Nusselt film thickness. For run 3S the fluid is silicone oil, $h^* = 0.69 \times 10^{-3}$ m, Re = 0.1284 and $Ca_m = 0.1052$. For run 16S the fluid is glycerin B, $h^* = 0.68 \times 10^{-3}$ m, Re = 0.0019 and $Ca_m = 0.0458$.

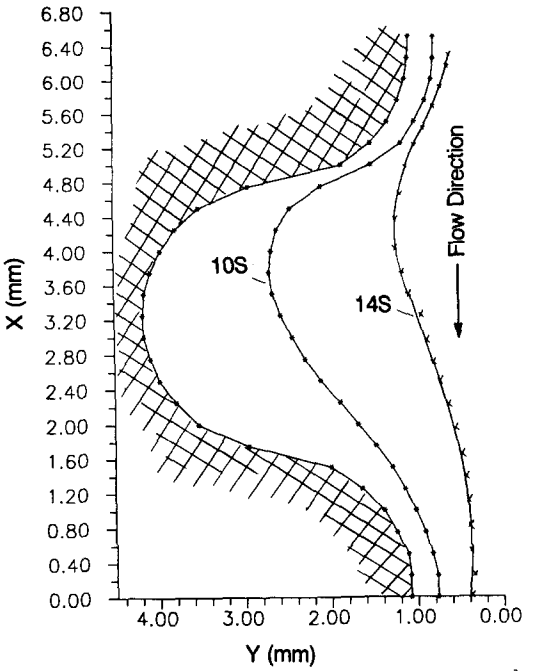

Figure 9. Film thickness data for two experimental runs with similar Re. For run 10S the fluid is silicone oil, $h^* = 0.22 \times 10^{-3}$ m, Re = 0.0043 and $Ca_m = 0.0109$. For run 14S the fluid is glycerin A, $h^* = 0.6 \times 10^{-3}$ m, Re = 0.0047 and $Ca_m = 0.036$.

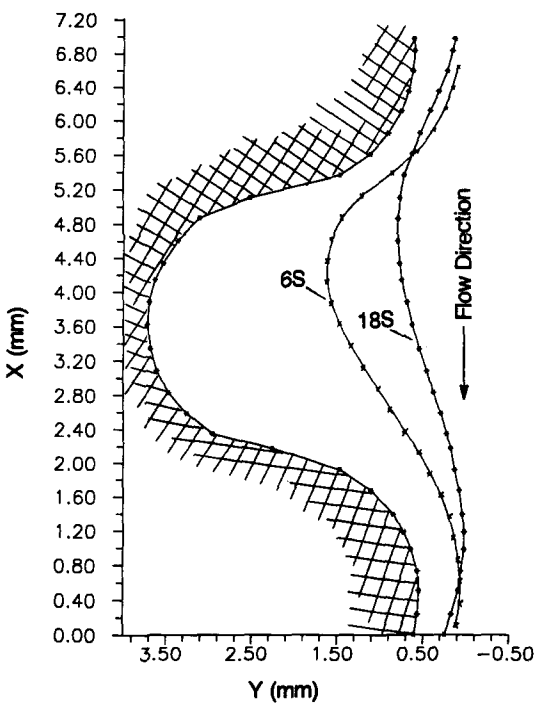

Figure 10. Film thickness data for two experimental runs with similar Ca. For run 6S the fluid is silicone oil, $h^* = 0.38\ 10^{-3}$ m, Re = 0.0221 and $Ca_m = 0.0326$. For run 18S the fluid is glycerin B, $h^* = 0.58$ m, Re = 0.0011 and $Ca_m = 0.0328$.

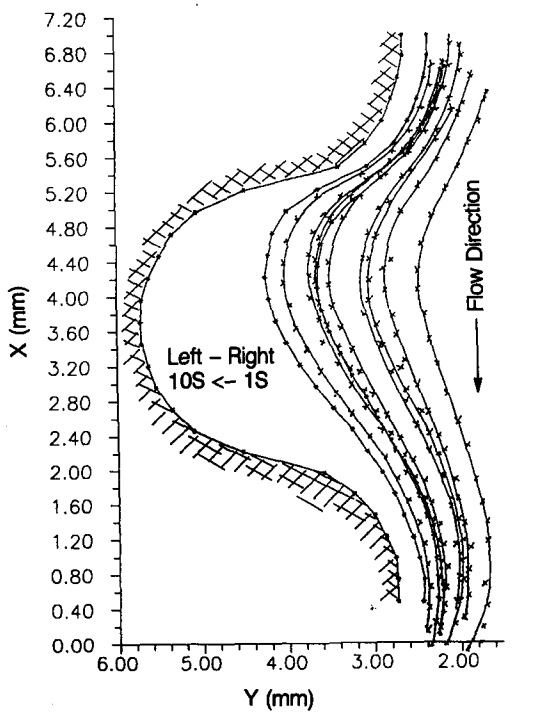

Figure 11a. Film thickness data for the flow of silicone oil on an S surface; $0.139 < \delta < 0.624$.

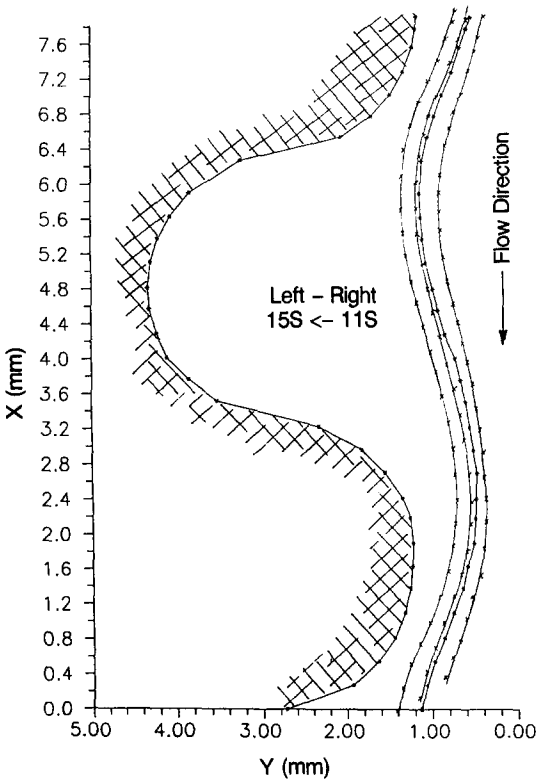

Figure 11b. Film thickness data for the flow of glycerin A fluid on an S surface; $0.139 < \delta < 0.624$.

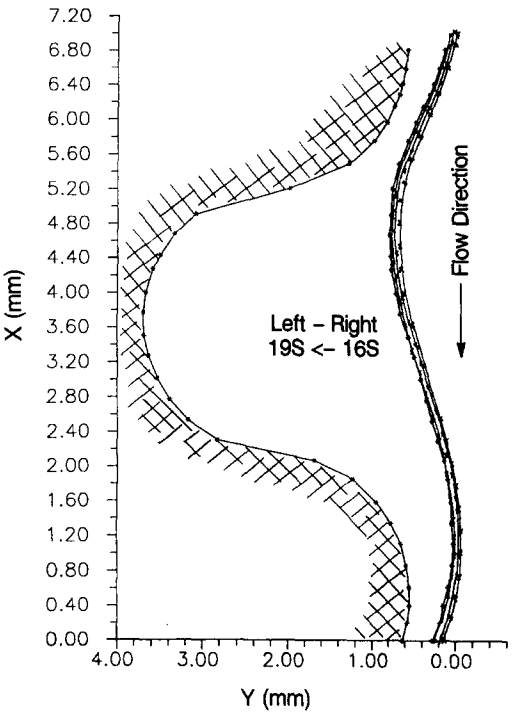

Figure 11c. Film thickness data for the flow of glycerin B fluid on an S surface; $0.139 < \delta < 0.624$.

for the flow of silicone oil and glycerin B over an S surface. In this case the Ca of the flow is kept nearly constant, while Re and the Nusselt film thickness are different. It is also obvious in this case, that Ca by itself will not be able to correlate experimental results.

The arrangement of all free-surface experimental data on S surfaces is shown in figure 11 for silicone oil (a), glycerin A (b) and glycerin B (c). A similar plot for the flow of silicone oil (a), glycerin B (b) and a 2:1 mixture of glycerin and water (c) on a C surface is shown in figure 12. Figure 13 shows similar data for silicone oil flowing on a T surface, while figure 14 shows the results for silicone oil (a) and a 2:1 mixture of glycerin and water (b) on a rod surface. Film thicknesses for all types of surfaces are thicker, on average, than the Nusselt film thickness for a vertical film predicted by [2]. However, in many cases there is a minimum film thickness that is smaller than

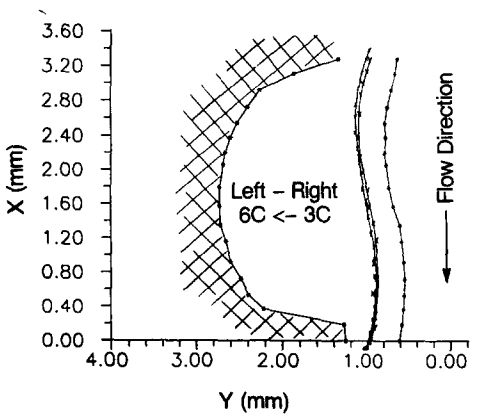

Figure 12a. Film thickness data for the flow of silicone oil on a C surface; $0.479 < \delta < 0.907$.

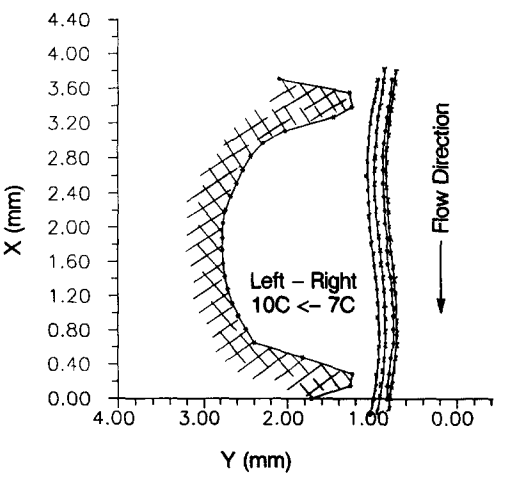

Figure 12b. Film thickness data for the flow of glycerin B on a C surface; $0.479 < \delta < 0.907$.

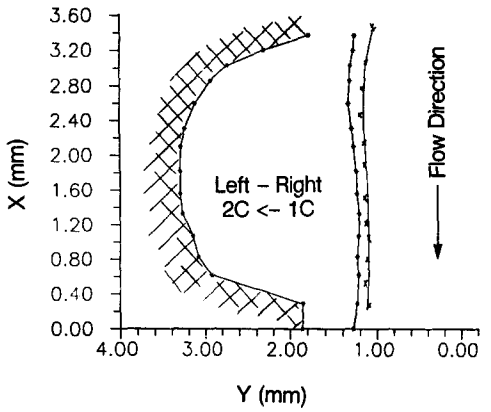

Figure 12c. Film thickness data for the flow of a 1:2 mixture of water–glycerin on a C surface; $0.479 < \delta < 0.907$.

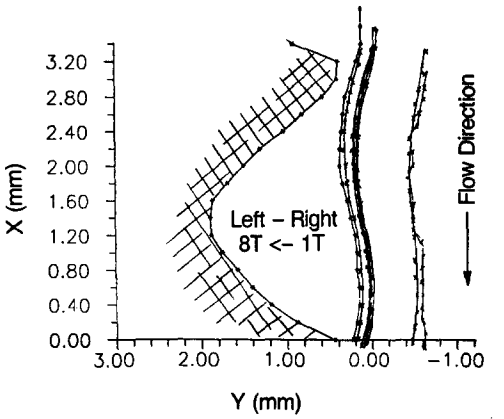

Figure 13. Film thickness data for the flow of silicone oil on a T surface; $0.252 < \delta < 1.272$. Notice that for larger values of δ the film is smoother but still periodic.

h^*. The only experiments where the liquid film thickness is $\geqslant h^*$ everywhere, are experiments with large ratios of film thickness/solid surface amplitude, i.e. for thick films. These results outline the rather complex nature of the balance of forces and of the accelerating–decelerating regions to be found along the surface profile.

The fully developed velocity profile for the laminar flow of a vertical falling film, described as Nusselt's flow, depicts a tight balance between viscous and gravity forces. This flow is totally specified if both the flow rate and the properties of the fluid are given. Shear stresses have a maximum at the solid wall and decreases to zero at the free surface. At each point of the parabolic velocity profile shear stresses support the weight of the outer layers of fluid. Abrupt changes in film thickness, following the contour of the complex surface, generate unbalanced stresses on the fluid that would accelerate and decelerate the outer fluid layers. Another important effect is due to the presence of a capillary pressure field that accelerates the liquid film beyond the acceleration due to gravity. In certain locations along the complex surface, the liquid film is concave prior to an inflexion point on the free surface and convex after it. The pressure inside the liquid film is greater than atmospheric pressure in regions with convex curvature and less in regions of concave curvature. As a consequence, a negative pressure gradient develops that increases the film average velocity. In a forthcoming paper (Zhao & Cerro 1992), the magnitude and direction of this pressure field are shown to have a strong influence on velocity profiles.

All free-surface profiles have the same wavelength as the solid surface. A changing flow rate results in changes in amplitude and phase shift. There are two ways to measure the amplitude and phase shift in these experimental surfaces. One way is to use the free-surface shape in laboratory

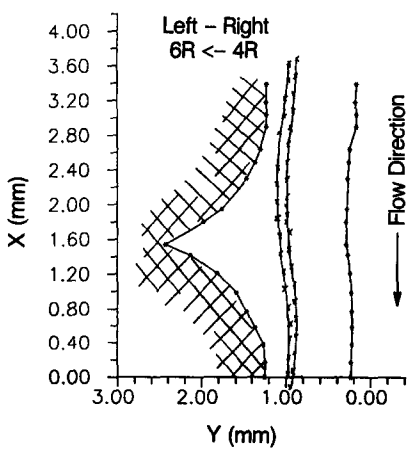

Figure 14a. Film thickness data for the flow of silicone oil on a rod surface; $0.264 < \delta < 1.159$.

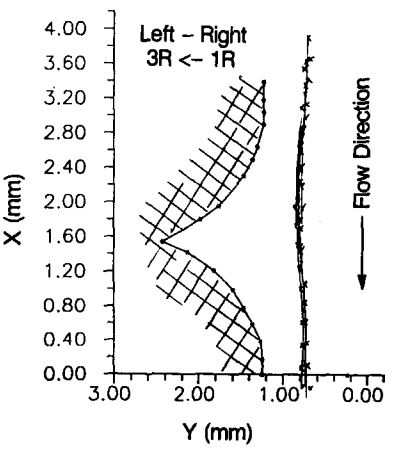

Figure 14b. Film thickness data for the flow of a 1:2 mixture of water–glycerin on a rod surface; $0.264 < \delta < 1.159$.

coordinates, i.e. as shown in figure 11. The other way is to use the film thickness as a function of position along the x-axis. The film thickness is the difference between the position measurement of the free surface and the position of the solid surface, both in laboratory coordinates. The amplitude of the liquid film profile is one-half the difference between the maximum and the minimum thickness of the periodic pattern. The amplitude ratios, β, are computed by dividing the experimental amplitude by the theoretical Nusselt film thickness, h^*:

$$\beta = \frac{h_{max} - h_{min}}{2h^*}, \qquad [6]$$

where h_{max} is the maximum film thickness or free-surface position and h_{min} is the minimum film thickness or free-surface position. The phase shift, ω, is the difference in degrees between the angular position of the minimum in the solid surface shape and the angular position of the minimum in the film surface pattern:

$$\omega = \theta_{fs} - \theta_{ss}, \qquad [7]$$

where θ_{fs} is the angular location of the minimum film thickness or free-surface position, and θ_{ss} is the angular location of the solid surface minimum. The phase shift and amplitude of the free surface are relevant to mass transfer processes. The phase shift and amplitude of the film thickness are relevant to film stability and dry-patch formation.

Experimental values of the phase shift and amplitude ratios for free-surface and film thickness measurements are shown in figures 15 and 16 as a function of h^* for **S**, **C**, **T** and **rod** surfaces. For **C**, **T** and **rod** surfaces, film thickness amplitude ratios are greater than free-surface amplitude ratios everywhere. For **S** surfaces, the amplitude ratio for the free surface is larger than the amplitude ratio of the film thickness for very small flow rates. The smallest values of δ were achieved with **S** surfaces, where $0.139 < \delta < 0.624$. On an **S** surface, for low flow rates a very thin film follows the contour of the surface such that the free surface will have an amplitude ratio close to the amplitude ratio of the solid surface, while the amplitude of the film thickness is relatively smaller. The maximum values of β for an **S** surface are, $\beta \gg 1$. In principle, as $h^* \to 0$, $\beta \to \infty$. Except for isolated regions along the solid surface profile, the film thickness is larger than h^*.

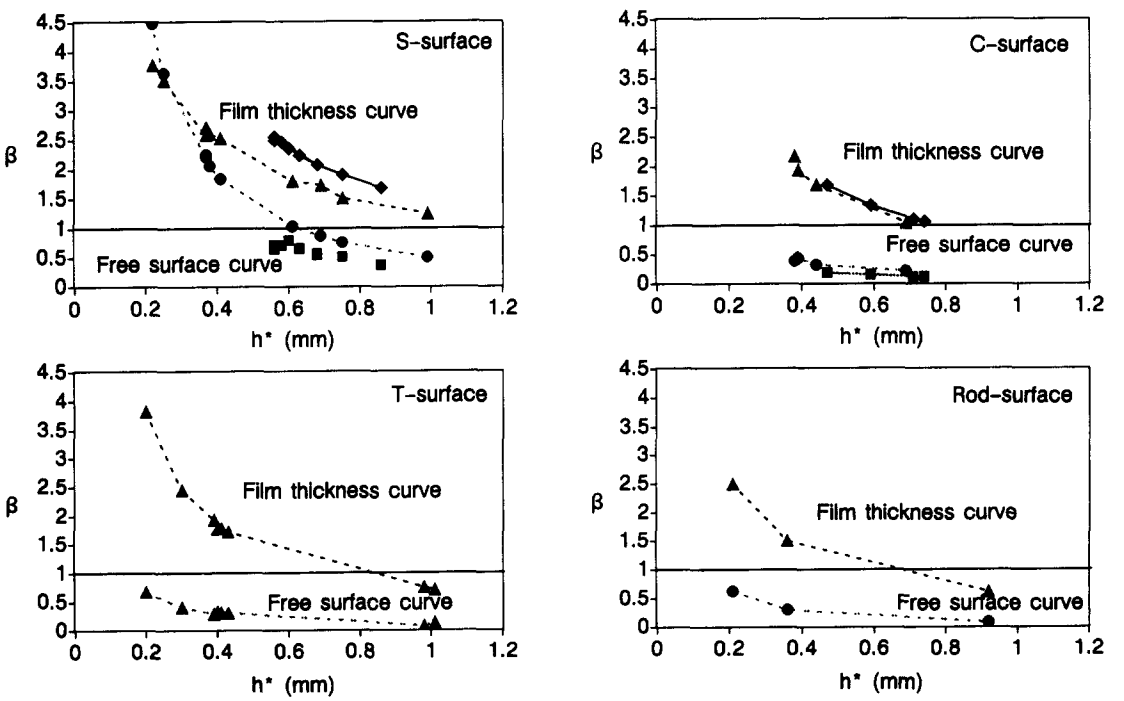

Figure 15. Amplitude ratio data for **S**, **C**, **T** and **rod** surfaces: ▲, film thickness curves, silicone oil; ●, free-surface curve, silicone oil; ◆, film thickness curves, glycerin; ■, free-surface curves, glycerin.

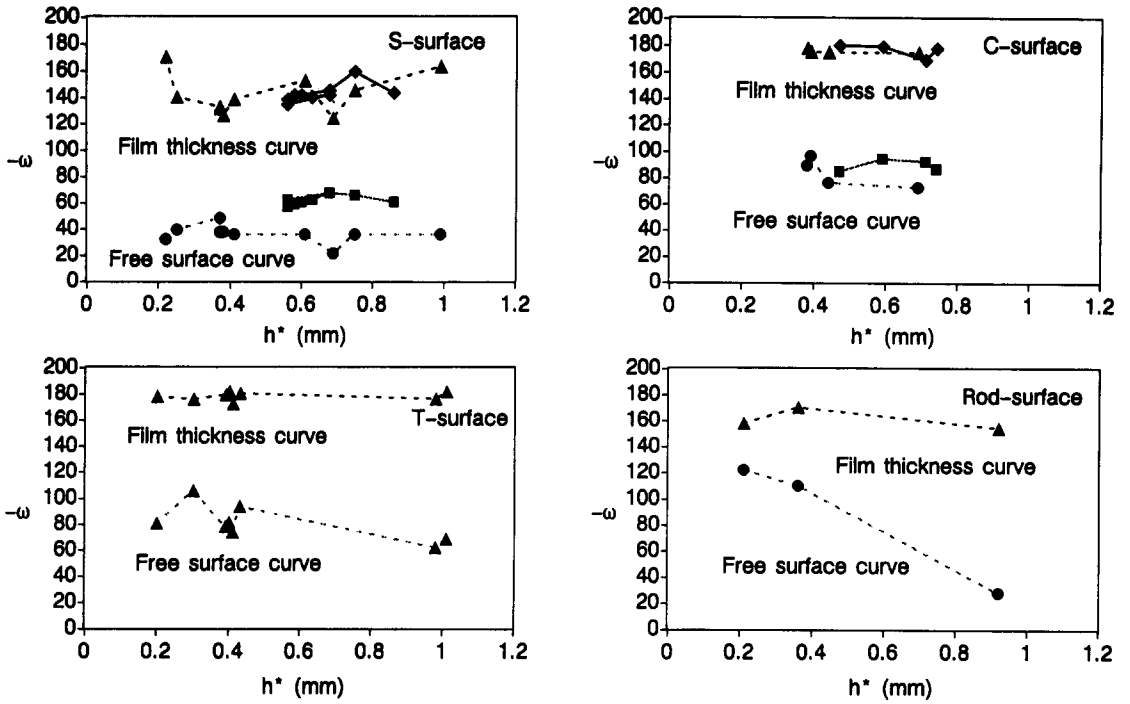

Figure 16. Phase shift data for S, C, T and **rod** surfaces: ▲, film thickness curves, silicone oil; ●, free-surface curve, silicone oil; ◆, film thickness curves, glycerin; ■, free-surface curves, glycerin.

As a consequence, the average film thickness is larger for the flow on a complex surface than its vertical falling film counterpart. For large flow rates, when $\delta > 1$, the free surface becomes nearly flat and the value of β for the free surface approaches zero, while the value of β for the film thickness approaches $1/\delta$.

The experimental values of the phase shift, ω, for free-surface and film thickness profiles are shown in figure 16. The phase shifts are remarkably constant for a wide range of film flow rates. The larger changes in values of ω are found in the free-surface measurements of the flow of silicone oil on a **rod** surface. Film thickness minimum values are, in general, found at or slightly downstream of the solid surface maximum ($\omega \sim -180°$). The film thickness minimum may or may not be smaller than the corresponding values of h^*. For an S surface, the film thickness minimum is, as an average, 40° downstream of the solid surface maximum. For C, T and **rod** surfaces the film thickness minimum is very close to the solid surface maximum. The free-surface minimum values are in general found in a position between the solid surface maximum ($\omega \sim 180°$) and minimum ($\omega \sim 0°$).

4. STREAMLINE PATTERNS

Streamlines, generated by the movement of brightly lit particles on a dark background, provide a revealing picture of the different flow patterns. There are two important characteristics of streamline patterns to point out: (1) the evolution of streamline shapes from the region close to the solid surface up to the free surface; and (2) the presence of recirculating or stagnation zones.

When there are no stagnation pockets, near the solid surface the shapes of the streamlines are very close to that of the solid surface. A typical pattern is shown in figure 17 for the flow of silicone oil on an S surface. There are no stagnation pockets in this pattern and the streamlines evolve smoothly from the sine-shape near the solid surface to the more complex free-surface shape. The streamline phase shift evolves from zero at the solid surface to a maximum negative value at the free surface. At this small Re (=0.0136), inertial forces are not large enough to affect the shape of the streamlines near the solid surface. Near the free surface, however, capillary forces dominate by reducing the curvature of the streamlines.

Some surfaces, such as the **S** surface and the industrial **P** surface, present no visible stagnation pockets for the whole experimental range of Re and Ca. Other surfaces, such as **rod** surfaces, present stagnation pockets even for the smallest Re. By contrast, **C** and **T** surfaces present stagnation pockets only for the highest range of Re and Ca. For **C** and **T** surfaces, decreasing flow rate reduces the size of the stagnation pockets down to a point where they disappear completely. Figure 18 shows a typical streamline pattern for a 1:1 mixture of glycerin and water flowing over a **rod** surface. The dark region near the cusp shows a tiny stagnation pocket. The presence of a stagnation pocket is delimited by a streamline that detaches from the solid surface on top and re-attaches to the solid surface at the bottom. The stagnation pockets persist even when the flow is completely cut-off. The fluid pockets remain at the line of contact between the rods and increase the static holdup of packings. This phenomenon is characteristic of certain industrial shapes made out of gauze or wire-mesh. Figures 19 and 20 show the streamline patterns for a **C** and a **T** surface, respectively. In both cases the fluid is silicone oil. The **C** surface, shown in figure 19, has a region of very slow flow in the lower section but no recirculation pattern. The **T** surface, shown in figure 20, has a region of slow flow at the interior corner but no recirculation pattern can be observed either.

5. FREE-SURFACE VELOCITIES

Figures 21 and 22 show dimensionless free-surface velocities for the flow of a 2:1 mixture of glycerin and water on a **rod** surface. Also shown in the figures are the solid surface profiles and free-surface and film thickness profiles for flows of similar characteristics. Due to the bulkiness of the film thickness measuring setup, it is impossible to make both the free-surface velocity and the film thickness measurements on the same surface location. Shown here, for the sake of comparison, are the film thickness measurements for flow $3R$ that has similar film thickness and Ca. The surface velocity minimum does not coincide with either the free-surface or film thickness maximum, but falls between the two. In an analogous way, the surface velocity maximum falls between the free-surface and film thickness minima. In both cases, maximum and minimum free surface velocities are shifted forwards with respect to the free surface extreme and backwards with respect to the film thickness extreme.

Dividing the experimental free-surface velocities by the theoretical Nusselt free-surface velocity, u_m^*, allows the presentation of these results in dimensionless form. Since u_m^* is computed using [2] and [3] for a flow with identical flow rate, it is a way to compare experimental values with what should be an upper bound for free-surface velocities if the velocity profiles were a sequence of fully developed Nusselt velocity profiles for different inclinations. This is not the case, since dimensionless free-surface velocities are shown in figures 21 and 22 to be, in some places, >1. This result is consistent with the observation that there are regions of flow on a complex surface where gravity and capillarity can accelerate the film beyond the maximum speed expected for a vertical Nusselt flow.

6. COMPARISON WITH EARLIER RESULTS

There is no data that the authors are aware of in the open scientific literature on the flow of liquid films over complex surfaces. The first theoretical treatment that the authors know of, of flows over wavy surfaces, i.e. surfaces with a sinusoidal shape, is due to Wang (1981). Wang (1981) allows the wavy plate to have striations along the x-axis and to be inclined with respect to the x- and z-axis. The resulting perturbation analysis is limited to small amplitudes of the wavy plate as compared to the average depth of fluid, i.e. $\delta \gg 1$. Asymptotic solutions have the same period as the wavy plate, while the amplitude and phase shift of the free surface depend on the wave and Weber numbers.

Pozrikidis (1988) introduced a boundary-integral computational analysis of the creep-flow equations of motion. This scheme can be used for surfaces of arbitrary shape, although in the paper reviewed (Pozrikidis 1988) the analysis is limited to a sinusoidal wall and to a wall with rectangular indentations. Inertial forces are neglected entirely. As a consequence, numerical solutions depend

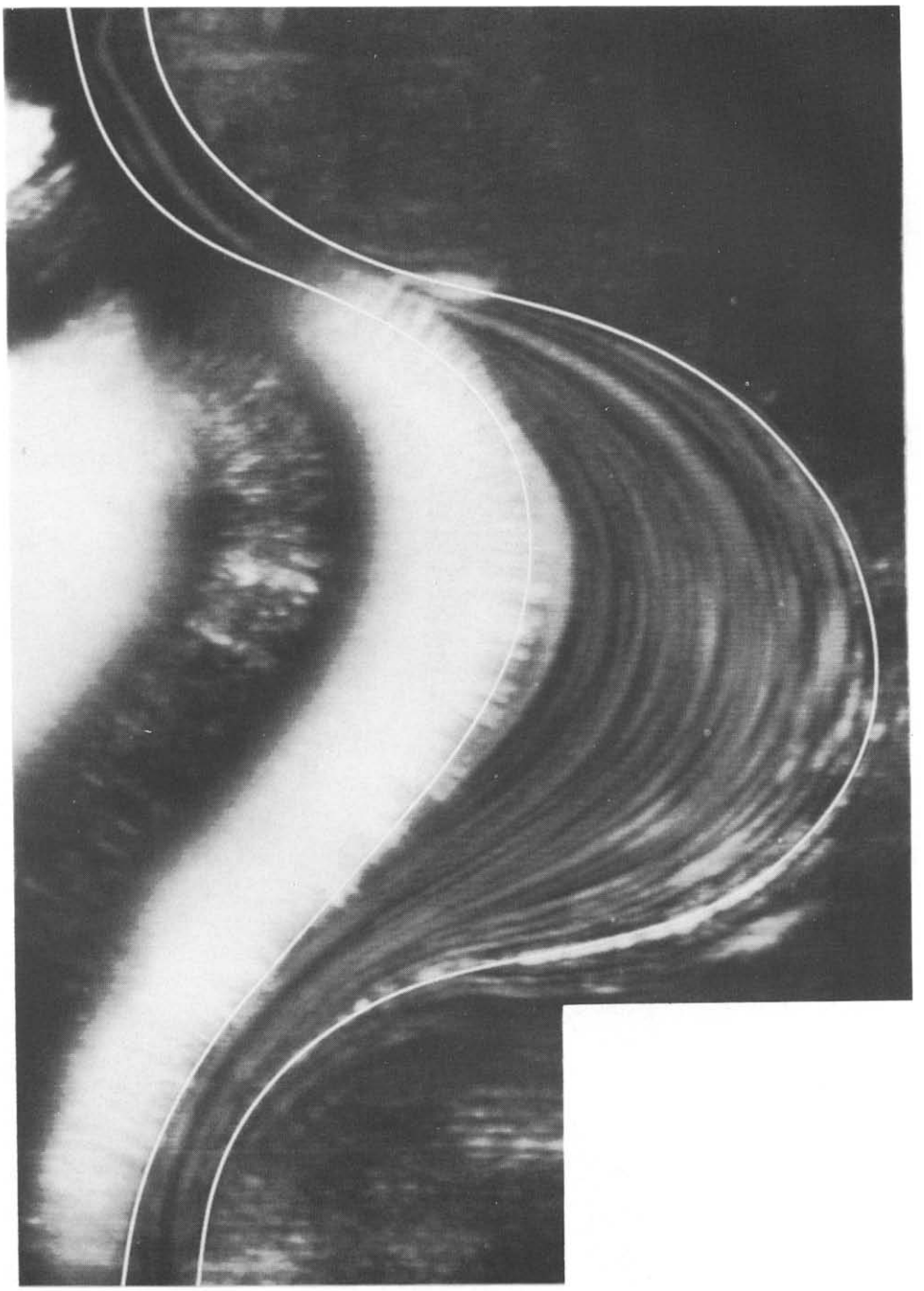

Figure 17. Streamline patterns for the flow of silicone oil on an S surface. Run 3S, $h^* = 0.69 \times 10^{-3}$ m, $\mathrm{Re} = 0.1284$ and $\mathrm{Ca_m} = 0.1052$.

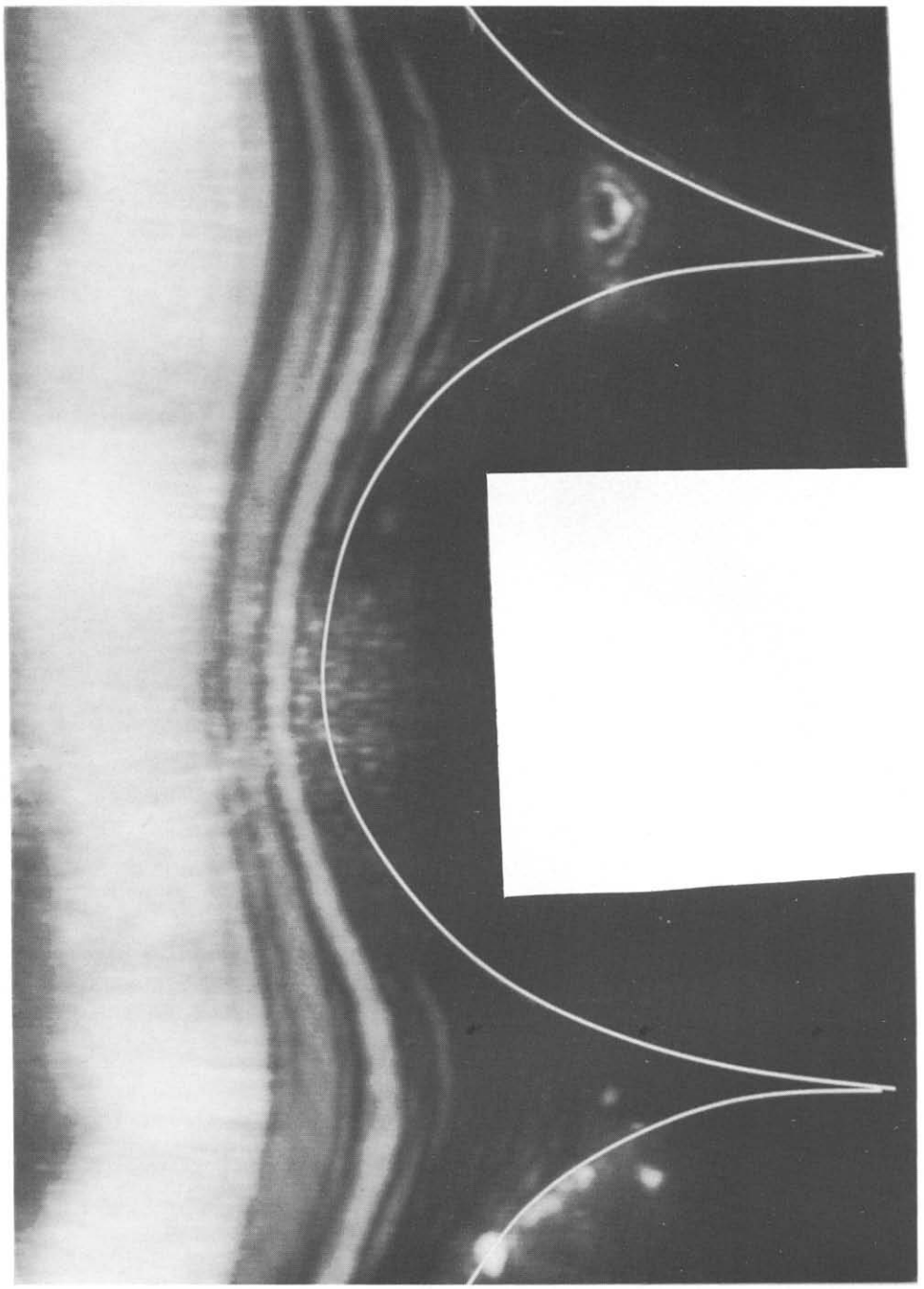

Figure 18. Streamline patterns for the flow of silicone oil on a **rod** surface. Run 5**R**, $h^* = 0.36 \times 10^{-3}$ m, Re = 0.0181 and $Ca_m = 0.0285$.

Figure 19. Streamline patterns for the flow of silicone oil on a T surface. Run 2T, $h^* = 0.98 \times 10^{-3}$ m, Re = 0.3678 and $Ca_m = 0.2122$.

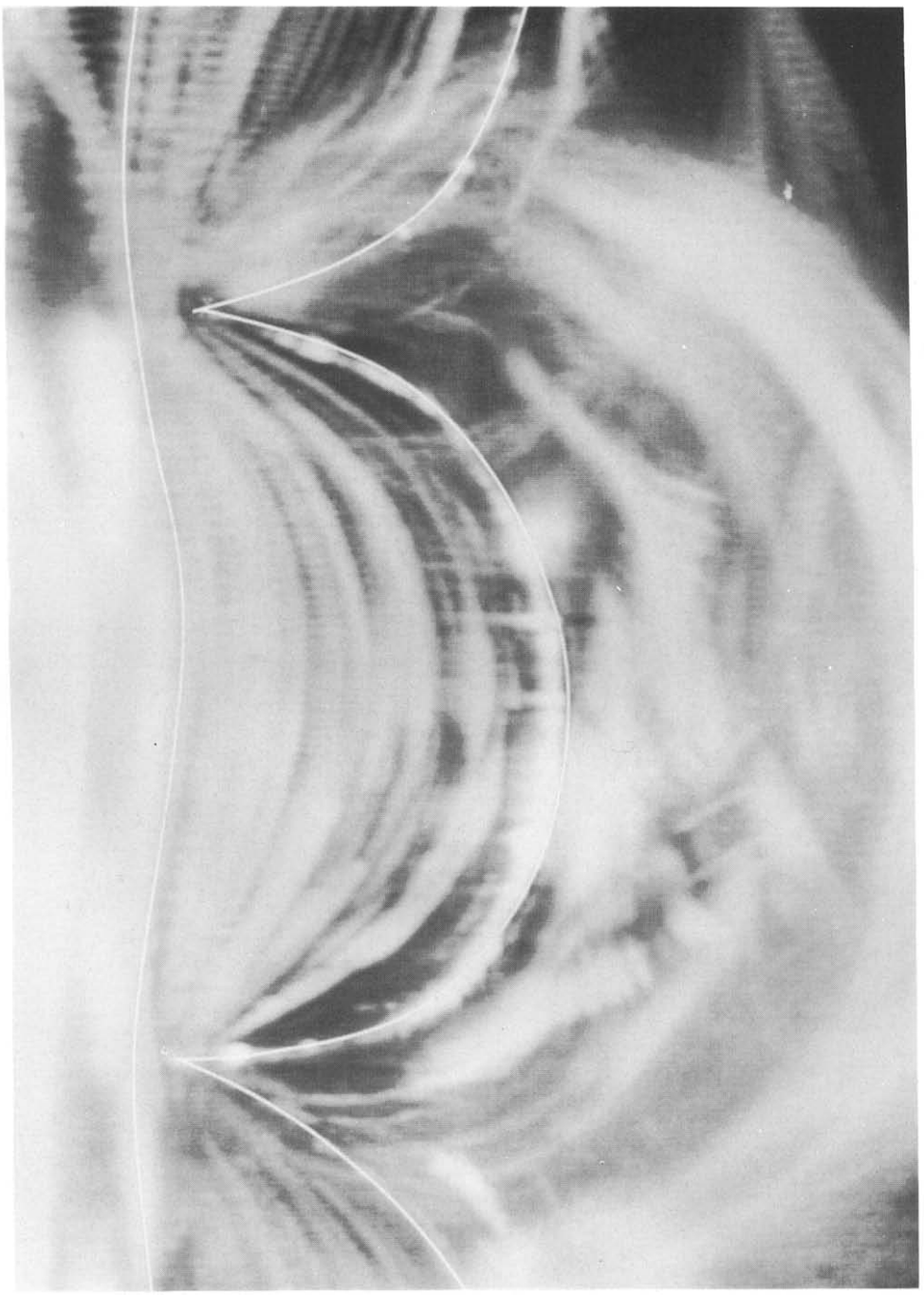

Figure 20. Streamline patterns for flow of a 1:2 mixture of water–glycerin on a C surface. Run 2C, $h^* = 0.65 \times 10^{-3}$ m, Re = 3.5 and $Ca_m = 0.0375$.

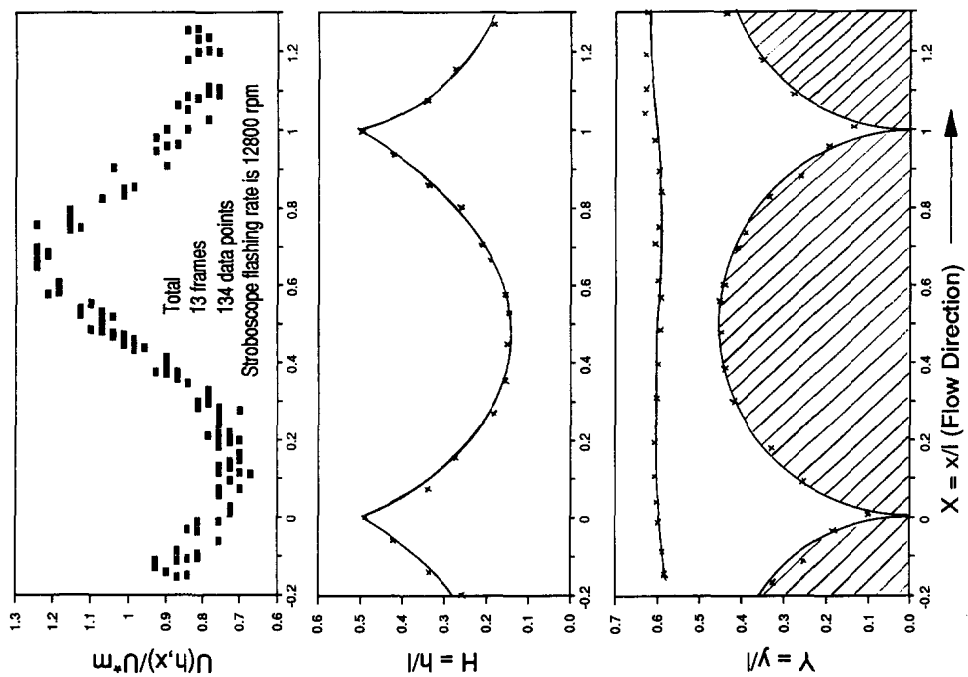

Figure 22. Free-surface velocity data for a 2:1 mixture of glycerin in water on a rod surface. $h^* = 0.523 \times 10^{-3}$ m, Re = 13.3 and $Ca_m = 0.022$. The film thickness data shown for comparison is run 3R, which has a similar film thickness and Ca.

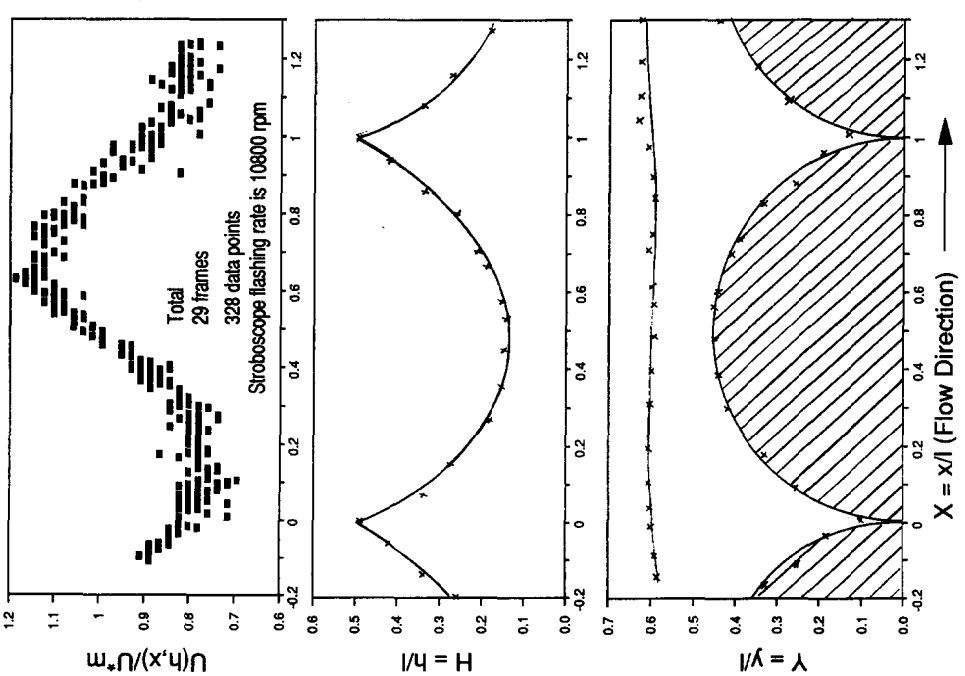

Figure 21. Free-surface velocity data for a 2:1 mixture of glycerin in water on a rod surface. $h^* = 0.492 \times 10^{-3}$ m, Re = 10.7 and $Ca_m = 0.0195$. The film thickness data shown for comparison is run 3R, which has a similar film thickness and Ca.

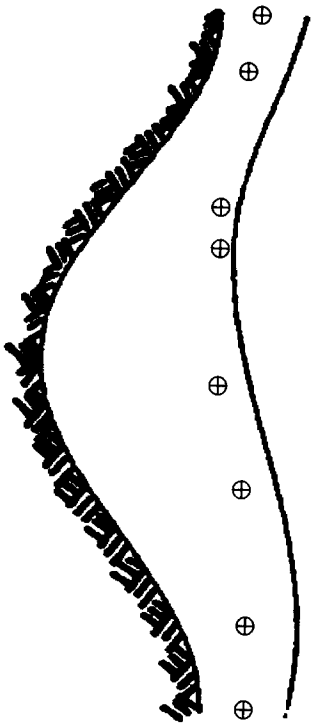

Figure 23. Comparison of experimental data with numerical data (Pozrikidis 1988). Pozrikidis's data (——) is for Bond number B = 0.2, $\lambda = 0.1$ and $h^*/b = 0.125$. The experimental data (⊕) is for B = 0.21, $\lambda = 0.25$ and $h^*/b = 0.11$. Also, the theoretical solid surface is a true sine wave curve.

on (our notation) the reduced wall amplitude, $A/b = \lambda$, the inclination angle α, the ratio of Nusselt film thickness/solid surface wavelength, $h^*/b = \delta/\lambda$, and a Bond number, defined by

$$\mathrm{B} = \frac{\rho g}{\sigma k^2}, \qquad [8]$$

where

$$k = \frac{2\pi}{b}. \qquad [9]$$

Few of Pozrikidis's (1988) computations are comparable to our own experimental results. Dimensionless numbers are the result of surface properties and experimental conditions that cannot be easily accommodated to fit arbitrary numerical data. The only numerical results that can be somehow quantitatively compared to our experimental results are shown in figure 12(d) of Pozrikidis (1988). Our closest experimental conditions are given in figure 11(c) for experiments 16S–19S, where the Bond numbers for glycerin B experiments are B = 0.211. Pozrikidis's (1988) reduced wall amplitude is $\lambda = 0.1$, while for all our experiments on S surfaces $\lambda = 0.25$. There is no close equivalent for the ratio of Nusselt film thickness/solid surface wavelength. Pozrikidis's (1988) values are $h^*/b = 0.239$, 0.125 and 0.057. Our closest value is $h^*/b = 0.11$ for experimental run 16S. A comparison of experimental run 16S with Pozrikidis's numerical data is shown in figure 23. The solid surface is a true sine function, while the experimental solid surface is a sequence of semi-circular grooves and ridges. As a consequence, experimental points near the inflexion of the solid surface do not compare well with the numerical results. A fairer comparison of Pozrikidis's (1988) numerical technique will require computations using parameters identical to our experimental parameters.

Qualitative comparisons are possible. Both Wang's (1981) and Pozrikidis's (1988) theoretical results include free surfaces that have the same period as that of the solid surface. This trend has been confirmed experimentally for intermediate to large values of δ. Free-surface amplitudes and phase shifts decrease as δ increases, as shown in figures 2 and 3 of Wang's (1981) paper and figures 5, 11 and 13 of Pozrikidis's (1981) paper.

7. CONCLUSIONS

Three parameters are needed to correlate the experimental data: (1) the Nusselt film thickness, h^*; (2) Re; and (3) Ca. These parameters represent three characteristic experimental effects: (1) the relative thickness of the liquid film with respect to the surface geometric parameters, highlighted by δ; (2) viscous effects, highlighted by Re; and (3) capillary effects, highlighted by Ca.

An arbitrary complex surface cannot be characterized by a single parameter. A regular periodic surface can be characterized by its amplitude and wavelength. All regular surfaces analyzed here have a constant amplitude/wavelength ratio, λ. Thus, experimental results need be related only to one surface geometric parameter. In this sense, it is equivalent in the presentation of results to use the Nusselt film thickness, the liquid flow rate or a ratio of these parameters to one of the geometric parameters. For the sake of clarity, and in order to make this data more readily available to other researchers, the experimental results are presented here as a function of h^*.

For large ratios of Nusselt film thickness/solid surface amplitude, i.e. $\delta > 1$, the liquid film presents a nearly flat free surface. For very small ratios, i.e. $\delta < 0.1$, liquid films follow the contour of the solid surfaces and approach the shape of quasi-fully-developed liquid films on inclined surfaces. The most interesting effects occur for ratios $0.1 < \delta < 1$. For the range of flow rates of industrial interest, the ratio of film thickness/surface amplitude, as an average, falls in the intermediate-to-large range for the *micro-structure*, i.e. $\delta \sim 1$, and in the intermediate-to-small range for the *macro-structure*, i.e. $\delta \sim 0.1$. Sections of packing poorly irrigated, however, will show film thickness/amplitude ratios clearly within the intermediate range.

Re values spanned over four orders of magnitude inside the laminar flow regime. Although the Re are very small, and in some cases well into what can be considered a *creep-flow* regime, it is clear that inertial forces cannot be neglected. Although the fluid velocity is generally small, streamlines have very small curvature radii. As a consequence, the kinetic energy of the fluid is small but inertial effects are not. Ca values spanned roughly two orders of magnitude and in all cases capillary forces are strong and cannot be neglected. These effects are definitively tied to the very small radii of curvature of the free-surface streamlines.

The shape of the solid surface is an important factor in the configuration of liquid film flow patterns. **Rod** surfaces have well-defined stagnation zones, while no stagnation pockets could be detected on **S** or **P** surfaces. Stagnation zones, especially when located in the inner regions of the solid surface, decrease the effective amplitude of the solid surface shape. As a consequence, the actual values of δ should be larger than the calculated values. Although no attempt was made here to analyze dry-patch formation, it is recognized that the micro-structure of the solid surface plays a crucial role in pinning the three-phase contact lines.

The flow characteristics of liquid films over complex surfaces of ordered packing materials must be analyzed from two complementary viewpoints: (1) overall mass transfer rates; and (2) formation of dry patches and dry-patch stability. Overall mass transfer rates, for a given multicomponent system, are functions of interfacial area and mean residence time. Interfacial area and residence time are related in a non-simple way to liquid holdup. In the analysis of mass transfer rates, it is assumed that the entire solid surface is covered by a liquid film, i.e. there are no dry patches. Dry patches are responsible for the loss of mass transfer area and, as a consequence, for the drop in mass transfer efficiency. The analysis of formation and stability of dry patches is outside the scope of this work.

For a viscous film completely covering a flat, vertical solid surface, the functional dependences of average film thickness and average free-surface velocities with flow rate were introduced in [1] and [2]. Film thickness increases with the cubic root of the flow rate, $h^* \sim q^{1/3}$, and free-surface velocity (and average velocity) increases with the 2/3 power of the flow rate, $u_m^* \sim q^{2/3}$. Liquid holdup is a direct function of liquid film thickness, thus $H \sim q^{1/3}$. Residence time is proportional to the ratio of liquid holdup/average velocity, $\Theta \sim q^{-1/3}$. As a consequence of these relationships, when the flow rate is increased the liquid holdup increases but the residence time decreases. Liquid film mass transfer coefficients for falling liquid films are strongly dependent on wave formation. Liquid films are inherently unstable and waves form at very small Re. The resulting relationship of the overall mass transfer rate with the flow rate is rather complex. Experimental reports (Vivian & Peaceman 1956) show an increase in the local mass transfer coefficient but a decrease in the contact time, with an overall decrease in the mass transfer rate.

For a generic complex surface, although a functional dependence among flow parameters may be similar to Nusselt's flow, the actual average film thickness and velocities can be substantially different. For all the geometrical configurations studied, the liquid film thickness is $>h^*$ at almost every position along the surface. If there are any points along the surface where the liquid film thickness is $<h^*$, these are short regions located around inflexion points of the free surface. These inflexion points, discussed in section 4, separate a flow region of high pressure from a flow region of low pressure and are responsible for free-surface velocities larger than those predicted by [2], for the same flow rate. Nevertheless, these regions of larger velocities and thinner films are small and very localized. As a result, the average film thickness of the liquid film on a complex surface is substantially larger and the average free-surface velocity substantially smaller than the film thickness and free-surface velocity for the Nusselt flow, with identical flow rate and flow properties. These facts have important consequences with respect to both mass transfer rates and film stability. Since the average film thickness is larger and the average velocities are smaller than the corresponding Nusselt's films, both liquid holdup and average residence time are larger for the complex surface than for the vertical film. Moreover, except for the small regions of maximum velocity, the film, due to its greater thickness, is less prone to breakup than its vertical counterpart.

Acknowledgements—The authors gratefully acknowledge support from the National Science Foundation, Division of Chemical, Biochemical and Thermal Engineering, Program on Fluid, Particulate, and Hydraulic Systems, Grant No. CTS-8912784, from the Office of Research of The University of Tulsa and from the Associate Dean for Research of the College of Engineering and Applied Sciences.

REFERENCES

ADRIAN, R. J. 1984 Scattering particle characteristics and their effect on pulsed laser measurements of fluid flow: speckle velocimetry vs particle image velocimetry. *Appl. Opt.* **23,** 1690–1691.

BRAVO, J., FAIR, J. R., HUMPHREY, J. L., MARTIN, C. L., SEIBERT, A. F. & JOSHI, S. 1984 Assessment of potential energy savings in fluid separations technologies: technology review and recommended research areas. Dept of Energy Report DOE/ID/12473D1.

CAMP, C. E., KOLB, W. B., SUBLETTE, K. L. & CERRO, R. L. 1990 The measurement of square channel velocity profiles using a microcomputer-based image analysis system. *Expts Fluids* **10,** 87–92.

FULFORD, G. D. 1964 The flow of liquids in thin films. *Adv. Chem. Engng* **5,** 151–236.

KURTZ, D. P., MCNULTY, K. J. & MORGAN, R. D. 1991 Stretch the capacity of high pressure distillation columns. *Chem. Engng Prog.* **Feb.,** 43–49.

MERZKIRCH, W. 1987 *Flow Visualization*, 2nd edn. Academic Press, New York.

POZRIKIDIS, C. 1988 The flow of a liquid film along a periodic wall. *J. Fluid Mech.* **188,** 275–300.

DE SANTOS, J. M., MELLI, T. R. & SCRIVEN, L. E. 1991 Mechanics of gas–liquid flow in packed-bed contactors. *A. Rev. Fluid Mech.* **23,** 233–260.

VIVIAN, J. E. & PEACEMAN, D. W. 1957 Liquid-side resistance in gas absorption. *AIChE Jl* **2,** 437–443.

WANG, C. Y. 1981 Liquid film flowing slowly down a wavy incline. *AIChE Jl* **27,** 207–212.

YANG, W. J. (Ed.) 1989 *Handbook of Flow Visualization.* Hemisphere, Washington, D.C.

ZHAO, L. & CERRO, R. L. 1988 Flow of a thin film over a complex surface. Presented at the *AIChE Natn. Mtg*, Washington, D.C.; *Session on Fundamental Research in Fluid Mechanics: Interfacial Flows.*

ZHAO, L. & CERRO, R. L. 1992 Computational analysis of liquid film flows over complex surfaces. In preparation.